

Sliding Gaussian ball adaptive growth: point cloud-based iterative algorithm for large-scale 3D photoacoustic imaging

Shuang Li^{1†}, Yibing Wang^{1†}, Jian Gao^{2†}, Chulhong Kim³,
Seongwook Choi³, Yu Zhang¹, Qian Chen¹, Yao Yao^{2*},
Changhui Li^{1, 4*}

^{1*}Department of Biomedical Engineering, College of Future Technology, Peking University, Beijing, China.

^{2*}School of Intelligence Science and Technology, Nanjing University, Suzhou, China.

³Department of Electrical Engineering, Convergence IT Engineering, Mechanical Engineering, and Medical Science and Engineering, Medical Device Innovation Center, Pohang University of Science and Technology, Pohang, Republic of Korea.

^{4*}National Biomedical Imaging Center, Peking University, Beijing, China.

*Corresponding author(s). E-mail(s): yaoyao@nju.edu.cn;
chli@pku.edu.cn;

Contributing authors: jaeger_ls@stu.pku.edu.cn; ddffwyb@pku.edu.cn;
jian_gao@smail.nju.edu.cn; chulhong@postech.edu;
swchoi715@postech.ac.kr; zyuaiyi1_@stu.pku.edu.cn;
chen_qian@stu.pku.edu.cn;

[†]These authors contributed equally to this work.

Abstract

Large-scale photoacoustic (PA) 3D imaging has become increasingly important for both clinical and pre-clinical applications. Limited by resource and application constrains, only sparsely-distributed transducer arrays can be applied, which necessitates advanced image reconstruction algorithms to overcome artifacts caused by using back-projection algorithm. However, high computing memory consumption of traditional iterative algorithms for large-scale 3D cases is practically unacceptable. Here, we propose a point cloud-based iterative algorithm

that reduces memory consumption by several orders, wherein a 3D photoacoustic scene is modeled as a series of Gaussian-distributed spherical sources. During the iterative reconstruction process, the properties of each Gaussian source, including peak intensities, standard deviations and means are stored in form of point cloud, then continuously optimized and adaptively undergoing destroying, splitting, and duplication along the gradient direction, thus manifesting the sliding ball adaptive growth effect. This method, named the sliding Gaussian ball adaptive growth (SlingBAG) algorithm, enables high-quality 3D large-scale PA reconstruction with fast iteration and extremely less memory usage. We validated SlingBAG algorithm in both simulation study and in vivo animal experiments. The source code for SlingBAG, along with supplementary materials and demonstration videos, will be made publicly available in the following GitHub repository: <https://github.com/JaegerCQ/SlingBAG>. The complete code and dataset will be uploaded upon acceptance of our paper.

Keywords: Iterative 3D PA reconstruction, Point cloud-based model, Gaussian ball representation, Sparse sensor distribution

1 Introduction

Photoacoustic imaging (PAI), which uniquely combines ultrasound detection and optical absorption contrast, is the only non-invasive optical imaging method that can image centimeters deep in living tissue with superior spatial resolution compared to other optical imaging techniques. PAI has been widely employed in various biomedical studies, including both pre-clinical animal studies and clinical studies [1]. As PAI technology continues to evolve, recent developments in three-dimensional (3D) PAI have further expanded its potential.

In recent years, significant progress has been made in the development of 3D PAI through the use of two-dimensional (2D) matrix arrays, demonstrating immense potential for in vivo applications, such as human peripheral vessel and small animal imaging. Various array configurations have been explored, ranging from spherical and planar arrays [2–9] to synthetic planar arrays that rely on scanning [10, 11]. However, limited by cost and technical difficulties, it is a great challenge to fabricate a matrix array that satisfies the spatial Nyquist sampling requirement for real-time large-scale 3D PAI, which typically requires tens of thousands or more transducer elements, as well as an equal number of parallel data acquisition channels. Therefore, real-time 3D PAI systems only have sparsely distributed sensors in reality, while it is well known that traditional back-projection image reconstruction methods will cause severe artifacts and a low signal-to-noise ratio (SNR) for extremely sparse arrays.

To address these challenges, researchers have employed iterative reconstruction (IR) methods to improve image quality with sparse sensor configurations.

One of the first iterative approaches to PAI was presented by Paltauf et al. [12], wherein the differences between observed and simulated projections were iteratively minimized to improve image quality. Subsequent iterative methods have incorporated various physical imaging factors. Wang et al. [13] demonstrated that iterative PLS

algorithms, with either quadratic smoothing or TV penalties, could enhance the performance of small animal 3D PAI systems. Similarly, Huang et al. [14] introduced forward and backward operators based on k-space pseudospectral methods. Although IR techniques have demonstrated superior performance for 2D PAI, for 3D PAI — where the spatial grid scale is substantially increased, the computational load and memory demands of 3D PAI IR reconstruction make these methods less feasible [13, 15, 16].

Efficient numerical implementations of adjoint operators for PAI reconstruction were introduced by Arridge et al. [17], who applied compressed sensing via Bregman iteration to reduce the required number of sensors. However, their approach was computationally intensive, limited to voxel counts on the order of 10^6 , and reliant on high-bandwidth probes not commonly used in modern systems. Hauptmann et al. [18] combined deep learning with IR by fitting gradient information via neural networks to reduce artifacts in limited-view reconstructions. However, this method required expensive retraining and suffered from limited generalizability. Shang et al. [15] approached the problem by creating a forward model using directly measured graphite point sources, but optimization inefficiencies and inaccuracies in the forward model hindered its practical application.

Recently, Huynh et al. [19] employed an iterative model-based reconstruction algorithm to achieve 3D PAI. However, their PAI system is based on a small transparent Fabry-Perot flat scanner, which can be very closely attached to the local flat tissue surface, substantially reducing the computing spatial space. This approach is not suitable for general large-scale 3D PAI for targets (like human thyroid tumors) with uneven outer surfaces. Additionally, they still require seconds to scan optical US sensors for one image acquisition, not a real-time PAI system.

Deep learning approaches for PAI reconstruction [18, 20, 21] offer improvements in computational efficiency and image quality, but they heavily rely on large, specialized training datasets, which can be difficult to obtain, and lack generalizability across different imaging systems or under varying conditions. This limits their broader applicability, particularly in diverse clinical settings where imaging conditions are not consistent.

Differentiable rendering technologies such as NeRF [22] and 3D Gaussian Splatting (3DGS) [23] tackle the similar challenge of reconstructing 3D imagery from sparse viewpoints. Differentiable rendering technology [24–28] enables self-supervised reconstruction of 3D scenes directly from scene observations, usually multi-view images. The photometric difference between the rendered image generated by the differentiable rendering pipeline and the actual captured image is utilized as a loss function, guiding the reconstruction of the entire scene through gradient back-propagation. NeRF, for instance, uses multi-layer perceptrons (MLPs) to map 3D spatial positions to colors and densities, while newer methods like InstantNGP use hash grids to store features at different spatial scales, allowing for faster and more memory-efficient reconstructions [29]. With advancements in this field, scene representation has shifted from implicit to explicit, accompanied by a progression from heavy neural network architectures to lightweight ones, or even none at all. Those pioneering works provide inspiration for PAI IR reconstruction.

Recently, PAI researchers have reported NeRF-based paradigms to perform 2D PAI image reconstruction [30]. However, MLP-heavy methods like NeRF, along with their reliance on dense sampling, are computationally prohibitive for large-scale 3D PAI.

In contrast to NeRF, 3D Gaussian Splatting (3DGS) [31] effectively addresses these computational challenges in 3D computer graphics. 3DGS applies object-order rendering by representing scenes as Gaussian ellipsoids, which are projected and composited onto a 2D screen using Elliptical Weighted Average (EWA) [32] for alpha blending. As a differentiable rendering strategy using explicit scene representation, 3DGS enables efficient, high-quality 3D reconstruction and real-time rendering.

Inspired by 3DGS, we propose the sliding Gaussian ball adaptive growth algorithm (SlingBAG) for 3D PAI reconstruction. Distinct from traditional voxel grids, this method stores PA source information in the form of point cloud that undergoes iterative optimization. Using a novel “differentiable rapid radiator” model, PA signals are synthesized from spatially distributed points, each represented as a Gaussian-distributed spherical PA source with specific peak intensity, standard deviation, and mean value. The Gaussian-distributed spherical PA source is then discretized into multiple concentric spheres, with each sphere’s radius and initial acoustic pressure determined by the discretized Gaussian distribution, making the PA forward process fully differentiable.

The forward model computes sensor signals, and by minimizing the discrepancies between synthesized and observed signals, we iteratively refine the point cloud, ultimately generating a voxel grid for the reconstruction result.

This work introduces the SlingBAG algorithm, detailing its differentiable rapid radiator, point cloud optimization, and physics-based point cloud-to-voxel shader. The proposed method is validated through both simulation and in vivo experiments. SlingBAG enables high-quality large-scale 3D PAI under sparse sensor distributions.

2 Results

2.1 High-Quality 3D PA Image Reconstruction under Extremely Sparse Planar Array

Here, we first used simulated hand vessels as the target tissue to demonstrate the high performance of the SlingBAG algorithm for reconstructing complex vascular systems. Based on the 3D imaging results of human peripheral hand vessels from previous work [10], we extracted voxel grids with 0.2 mm interval to create the peripheral hand vessels, which were used as the simulated acoustic source and ground truth (Fig. 1(a)) to validate our reconstruction method. At a grid size of 0.2 mm, the total gridding size of the imaging area was $400 \times 520 \times 200$ (80 mm \times 104 mm \times 40 mm). For the planar PA detection matrix, we uniformly placed 122,500 sensors (350×350 , with a pitch of 0.4 mm) on a plane covering 140 mm \times 140 mm area, and the plane of the matrix array is about 15 mm below the imaging area (Fig. 1(j)).

For sparse detector arrangements, we undersampled the original 122,500 sensors into four different sparse matrix distribution alignments with sensor numbers of 49, 196, 576, and 4900, respectively. The pitches between adjacent sensors in these four different configurations are 20 mm, 10 mm, 6 mm, and 2 mm, respectively. For each

configuration, both the UBP algorithm and the SlingBAG algorithm were performed for comparison.

The reconstruction results are shown in Fig. 1(b-i). For each group of images, the three sub-images from top to bottom respectively show the Top-view maximum amplitude projection (MAP), Front-view MAP, and a slice along the green dashed line in the Top-view MAP of the 3D reconstruction result. More 3D reconstruction results using both algorithms with different array configurations can be found in Supplementary Video 1-3.

Under extremely sparse sensor configurations, the UBP reconstruction results contain serious artifacts (Fig. 1(b-d)), whereas the SlingBAG algorithm demonstrates remarkable 3D reconstruction capability (Fig. 1(f-h)); it even reconstructs the outline of the hand vessels with only 49 sensors. As the sensor matrix becomes denser, the quality of SlingBAG’s reconstruction improves rapidly. With 576 sensors, SlingBAG already achieves high-quality reconstruction, whereas the UBP results still exhibit severe artifacts (Fig. 1(d)(h)). When with a total of 4900 sensors, the SlingBAG reconstruction (Fig. 1(i)) is nearly identical to the ground truth (Fig. 1(a)). In contrast, the UBP result (Fig. 1(e)) remains blurry due to reconstruction artifacts, making it difficult to discern fine vascular details (marked by the white dotted box). Notably, even when using all 122,500 sensors for UBP reconstruction (Supplementary Fig. 3(b)), the result still cannot match the quality of SlingBAG reconstruction with only 4900 sensors. This is because the finite size of the detection matrix array caused the so-called “limited view” problem. However, despite the limited view condition, the SlingBAG algorithm performs exceptionally well, which is another advantage of the IR algorithm.

In Fig. 1(k), we plotted the normalized signal intensity distribution along the yellow dashed line in the slice images for comparison (the dashed line’s length does not represent the horizontal axis of the curve). The green solid line represents the intensity distribution of the ground truth, the red dashed line represents the intensity distribution of the reconstruction result from 4900 sensors, and the blue dashed line represents the intensity distribution from 576 sensors. As the number of sensors increases from 576 to 4900, the intensity distribution along the yellow dashed line in the slice progressively approximates the true value. The discernibility of several “peaks” in the intensity distribution also significantly improves, indicating that the SlingBAG algorithm’s reconstruction accuracy is strongly positively correlated with the density of sensor distribution.

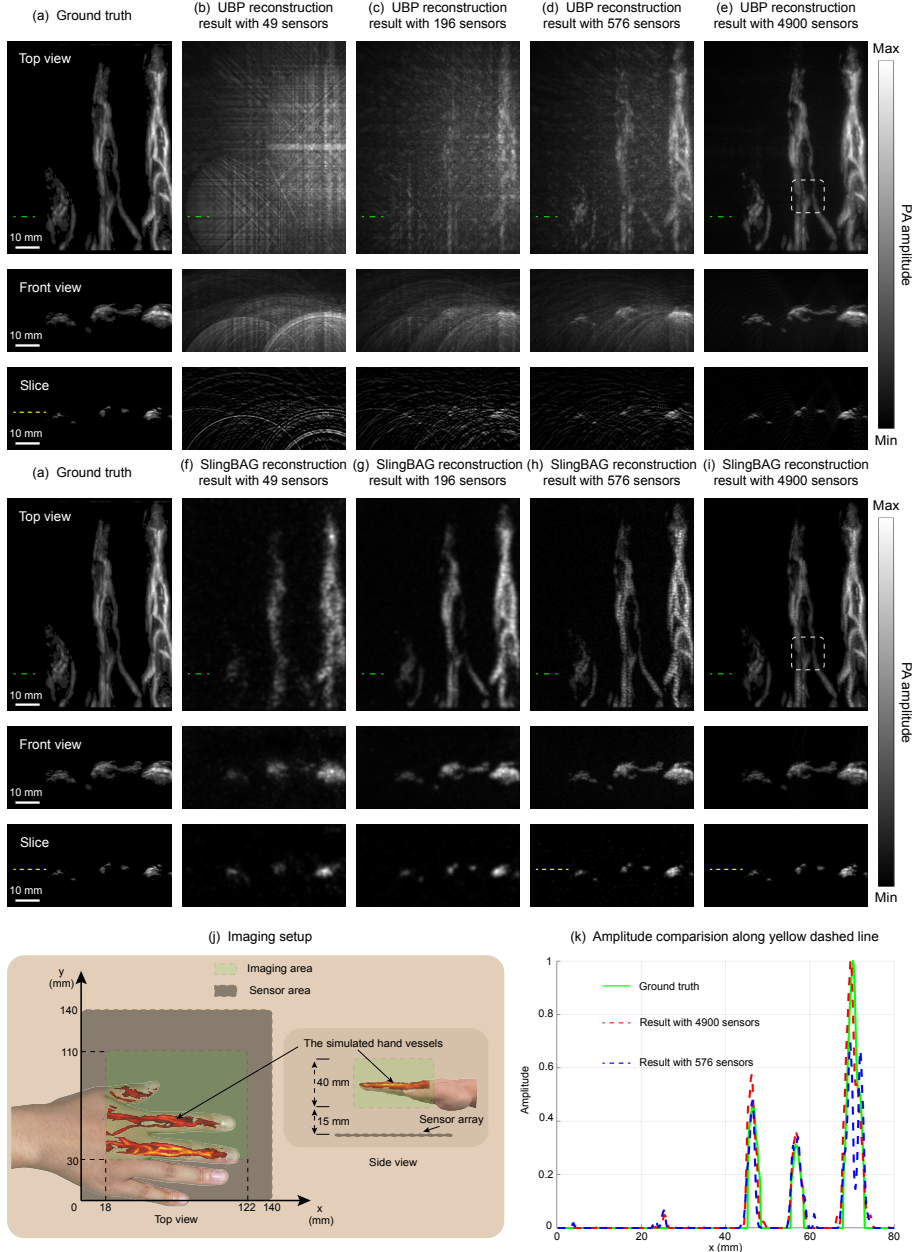


Fig. 1 Comparison of 3D photoacoustic reconstruction results under extremely sparse planar arrays. (a) Top-view maximum amplitude projection, front-view maximum amplitude projection, and slice at the green dashed line in the top-view-MAP of the acoustic source. (b-e) Top-view maximum amplitude projection, front-view maximum amplitude projection, and slice at the green dashed line in the top-view-MAP of the UBP reconstruction result with 49, 196, 576 and 4900 sensors. (f-i) Top-view maximum amplitude projection, front-view maximum amplitude projection, and slice at the green dashed line in the top-view-MAP of the SlingBAG reconstruction result with 49, 196, 576 and 4900 sensors. (j) Imaging setup. (k) Intensity distribution curves along the yellow dashed line in the vertical coordinate of the slices from the acoustic source, 576-sensor reconstruction, and 4900-sensor reconstruction. (Scale: 10 mm.)

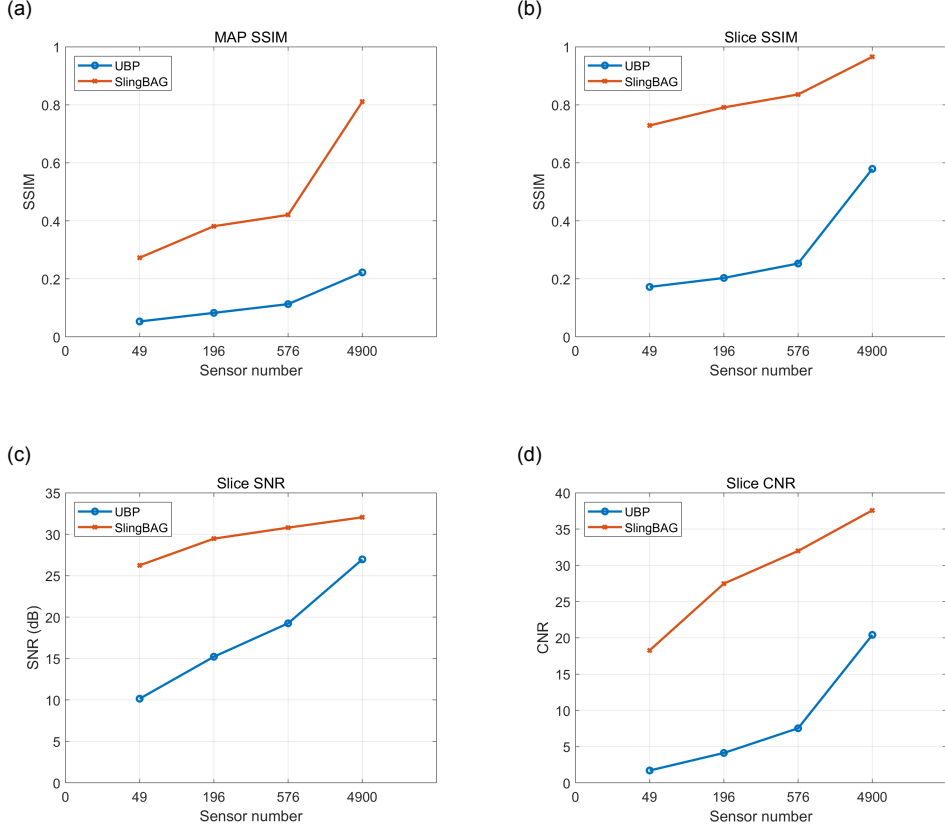


Fig. 2 Assessment for image quality of 3D photoacoustic reconstruction results under extremely sparse planar arrays. (a) Structural similarity index (SSIM) of the Top-view maximum amplitude projection of the reconstruction results. (b) Structural similarity index (SSIM) of the slice of the reconstruction results. (c) The signal-to-noise ratio (SNR) of the slice of the reconstruction results. (d) The contrast-to-noise ratio (CNR) of the slice of the reconstruction results.

We used the structural similarity index (SSIM) of the Top-view maximum amplitude projection (MAP), the SSIM of the slice, the contrast-to-noise ratio (CNR), and the signal-to-noise ratio (SNR) (Fig. 2) to quantitatively assess the reconstruction results of the SlingBAG and UBP algorithms under different sensor configurations. In the SSIM line graph for the Top-view MAP, for the reconstruction using 4900 sensors, the UBP algorithm achieves only a score of 0.22, whereas the SlingBAG result reaches 0.81. This directly reflects the high fidelity of the 3D reconstruction by SlingBAG, indicating a much greater overall accuracy than UBP. The SSIM line graph for the slice similarly shows that under the same sensor configurations, SlingBAG has an unparalleled advantage in reconstructing vascular details, achieving an SSIM of 0.84 with just 576 sensors, while the UBP result under the same conditions falls below 0.3. When the number of sensors reaches 4900, the SSIM of SlingBAG for the slice hits 0.97, effectively indicating a complete restoration of the vascular structure of

the acoustic source. Additionally, Fig. 2(b-c) shows that the SlingBAG reconstruction results exhibit significantly higher contrast-to-noise ratio (CNR) and signal-to-noise ratio (SNR) compared to the UBP results. In the case with 4900 sensors, the CNR of the SlingBAG result reaches approximately 40.

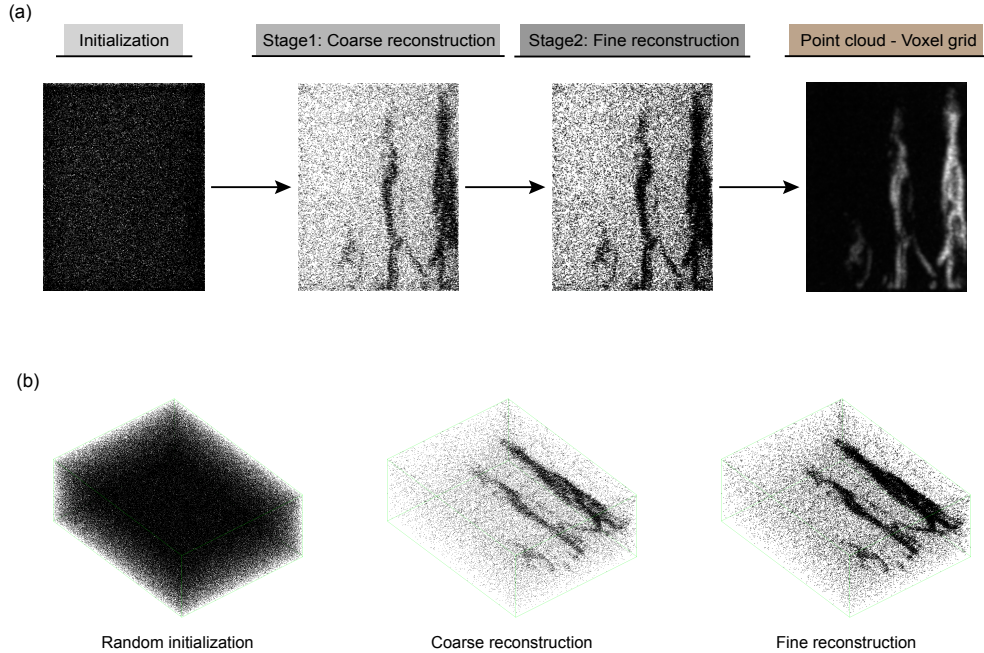


Fig. 3 Visualization of iterative reconstruction results. (a) Visualization of initialization point cloud, coarse reconstruction point cloud, fine reconstruction point cloud and the final voxel grid reconstruction result. (b) 3D visualization of point clouds at various stages of the entire reconstruction process, including random initialization, coarse reconstruction stage, and fine reconstruction stage.

We further visualized the iterative results of our reconstruction algorithm’s point cloud for the 196-sensor array in Fig. 3. We first initialized a relatively dense point cloud distribution randomly within the reconstruction region. Then, at the coarse reconstruction stage, both the position update and point duplication were disabled, only the peak initial pressure and standard deviations of each Gaussian ball underwent updates. Then, we got an initial convergence result in the coarse reconstruction stage.

Next, we enabled the model’s position update and point cloud duplication features in the fine reconstruction stage. It can be seen that the converged shape of the three finger vessels in the coarse reconstruction gradually becomes denser, along with finer details becoming clearer (Fig. 3(a)). Fig. 3(b) shows the 3D visualization results of the point cloud throughout the entire reconstruction process, from random initialization to coarse reconstruction result and finally to fine reconstruction result. Furthermore, through our point cloud-to-voxel grid shader, we transformed the fine reconstruction

result from point cloud form into voxel grid (Fig. 3(a)). More detailed visualizations of the intermediate iterative process can be found in Supplementary Fig. 8.

2.2 3D image reconstruction of in vivo mouse brain, rat kidney and rat liver

Then, we performed image reconstruction of real mouse and rat experimental data using both the UBP and the SlingBAG algorithms. The in vivo animal study data, including mouse brain, rat kidney and rat liver, was acquired by researchers in Kim’s lab using a 1024-element hemispherical ultrasound (US) transducer array with a radius of 60 mm [33]. Each US transducer element in the array had an average center frequency of 2.02 MHz and a bandwidth of 54%. The effective field of view (FOV) was 12.8 mm \times 12.8 mm \times 12.8 mm, and the spatial resolutions of approximately 380 μ m were nearly isotropic in all directions when all 1024 US transducer elements were used [33]. More information regarding the PAI system can be found in Kim’s publications [33–37].

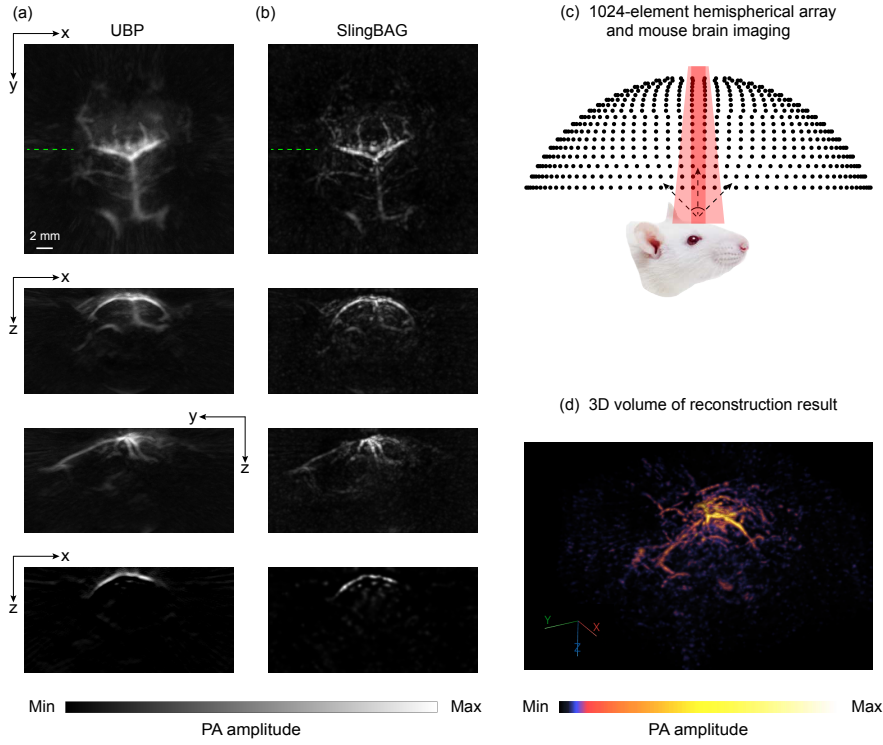


Fig. 4 Mouse brain 3D photoacoustic reconstruction results. (a) XY Plane-MAP, XZ Plane-MAP, YZ Plane-MAP and slice at green dashed line in XY Plane-MAP of the UBP 3D reconstruction results using 1024 sensor signals. (b) XY Plane-MAP, XZ Plane-MAP, YZ Plane-MAP and slice at green dashed line in XY Plane-MAP of the SlingBAG 3D reconstruction results using 1024 sensor signals. (Scale: 2 mm.) (c) Schematic diagram of the hemispherical array imaging the mouse brain. (d) 3D volume of SlingBAG reconstruction result.

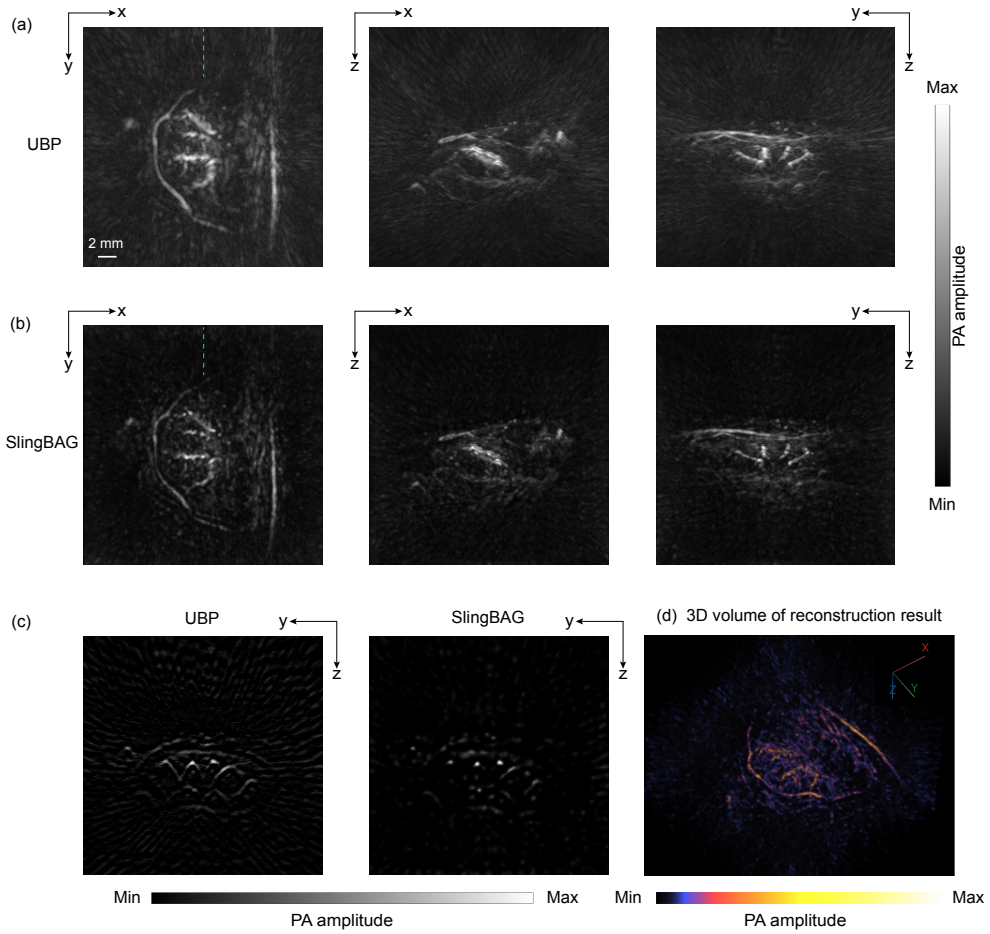


Fig. 5 Rat kidney 3D photoacoustic reconstruction results. (a) XY Plane-MAP, XZ Plane-MAP, and YZ Plane-MAP of the UBP 3D reconstruction results using 1024 sensor signals. (b) XY Plane-MAP, XZ Plane-MAP, and YZ Plane-MAP of the SlingBAG 3D reconstruction results using 1024 sensor signals. (c) Slice at green dashed line in XY Plane-MAP of 3D reconstruction results using 1024 sensor signals with different algorithms. (Scale: 2 mm.) (d) 3D volume of SlingBAG reconstruction result.

First, we compared the UBP and SlingBAG reconstruction results for a mouse brain using 1024 array elements (Fig. 4). In Fig. 4(a), from top to bottom, the images show the MAP results in XY Plane, XZ Plane, and YZ Plane, respectively, as well as a slice of the UBP reconstruction. Fig. 4(b) presents counterpart results by the SlingBAG algorithms. The 3D SlingBAG reconstruction result in Fig. 4(d) is available online (Supplementary Video 4). According to results, the SlingBAG reconstruction exhibits minimal artifacts and reveals far more vascular details compared with the UBP results. While in the UBP result, due to artifacts induced by sparse sensors, the vascular cross-sections are almost indiscernible. Further analysis showed that the contrast-to-noise ratio (CNR) of the UBP reconstruction was 10.60, whereas the CNR of the SlingBAG

reconstruction reached 61.55, demonstrating the SlingBAG algorithm's superior noise suppression capability.

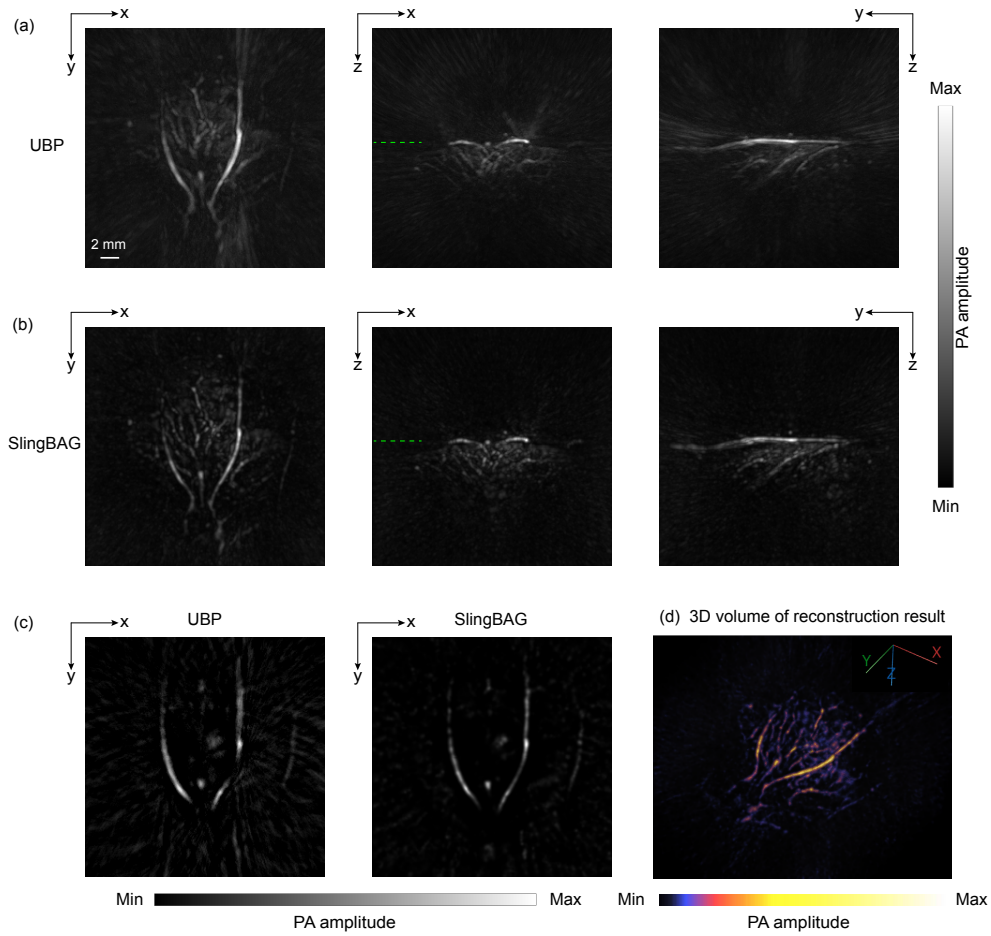


Fig. 6 Rat liver 3D photoacoustic reconstruction results. (a) XY Plane-MAP, XZ Plane-MAP, and YZ Plane-MAP of the UBP 3D reconstruction results using 1024 sensor signals. (b) XY Plane-MAP, XZ Plane-MAP, and YZ Plane-MAP of the SlingBAG 3D reconstruction results using 1024 sensor signals. (c) Slice at green dashed line in XZ Plane-MAP of 3D reconstruction results using 1024 sensor signals with different algorithms. (Scale: 2 mm.) (d) 3D volume of SlingBAG reconstruction result.

Additionally, in Fig. 5 and Fig. 6, we presented the reconstruction results of a rat kidney and a rat liver, respectively. In the slice view of the reconstructed kidney image in Fig. 5(c), the UBP results show severe arc-shaped artifacts caused by sparse sensor configuration and limited view issue, which significantly impair the ability to resolve the fine vascular structures. In contrast, the SlingBAG algorithm effectively suppresses these arc-shaped artifacts, producing a much clearer and cleaner vascular

cross-sectional image. Similarly, the SlingBAG algorithm renders the liver vessels with much better continuity, and much fewer artifacts. The 3D reconstruction results in Fig. 5(d) and Fig. 6(d) can be found in Supplementary Video 5 and Supplementary Video 6. For a quantitative comparison, the CNR by the UBP reconstruction for the kidney and liver are 21.56 and 17.48, respectively, whereas they are 58.15 and 48.57 for SlingBAG results. These results illustrate the exceptionally high quality of image reconstruction achieved by the SlingBAG algorithm.

2.3 Computing memory consumption analysis and comparison

Besides the quality of image reconstruction, the demand of computing memory usage is also a key role for practical implementation. Here, we compared the computing memory consumption of our SlingBAG algorithm with that of traditional iterative algorithms under the same experimental setup.

In the hand vessels reconstruction experiment using a planar matrix array, and with 4,900 sensors, the forward simulation combined with the backward gradient propagation of the SlingBAG algorithm required only 3.56 GB of memory. In comparison, the theoretical memory consumption of traditional iterative methods, such as k-Wave and the Fast Iterative Shrinkage-Thresholding Algorithm (FISTA) [38], is estimated to be as high as 19.32 GB, which exceeds the memory capacity limits of many consumer-grade GPUs. In the *in vivo* animal imaging experiment using a hemispherical array, the forward simulation combined with the backward gradient propagation of the SlingBAG algorithm required only 2.99 GB of memory. In comparison, traditional iterative methods require the use of a large spatial grid to accommodate the hemispherical array, leading to an estimated astonishing memory consumption of 85.89 GB, making it virtually impractical for most of accessible consumer-level GPU resources. More details of theoretical analysis for memory demand by traditional IR methods are provided in the Supplementary Note 7.

3 Discussion

Real-time large-scale 3D PA imaging using sparsely distributed detectors has garnered significant attention. However, traditional IR reconstruction methods face great challenges due to their extremely large amount demand of GPU memory. This work proposes SlingBAG, a point cloud iteration-based 3D PA imaging reconstruction algorithm, which substantially increases speed with much less memory consumption. We have validated its effectiveness in achieving high-quality 3D reconstructions under extremely sparse sensor distributions using both simulated data and real experimental data from *in vivo* animal studies. The SlingBAG algorithm provides substantially higher reconstruction quality than UBP, effectively suppressing reconstruction artifacts.

Compared with traditional IR methods, the SlingBAG reconstruction method has two key advantages: much less memory consumption and fast reconstruction speed.

The simulated hand vessels data spans dimensions of 40 mm \times 104 mm \times 80 mm in physical space. In traditional voxel grids, using a 0.2 mm grid interval results in a

gridding size of $200 \times 520 \times 400$. Using signal data from 196 sensors for sparse reconstruction, with each sensor having 4096 sampling points at a 40 MHz sampling frequency, the data volume is nearly impractical for traditional voxel-based IR methods in terms of memory usage and time consumption. However, our method only requires less than 3 GB of GPU memory. Regarding the widely used forward model k-Wave, its k-space pseudo-spectral method’s memory consumption heavily depends on the defined spatial grid size. Although traditional IR methods with powerful tools like k-Wave have shown superior performance in PA 2D imaging, the computing memory usage for the 3D case increases exponentially. Additionally, in iterative algorithms, this imposes a significant memory burden on gradient computation and optimizers, which is unacceptable for most research laboratories.

Moreover, concerning computational time consumption, k-Wave, as well as other tools that numerically solve PA wave functions in the time domain, requires computing the acoustic field at each time step over entire spatial grids, which is extremely time-consuming when for large-scale PA imaging. However, our method can directly calculate the far-field acoustic field for the forward model. For the mentioned spatial grid, 196 sensors, and 4096 time steps, using the same RTX 3090 Ti GPU, the forward process in our method takes only 15 seconds with a point cloud with 600,000 sources. In contrast, k-Wave takes more than 1000 seconds, making it more than 55 times slower than our method. The complete 3D image reconstruction with 196 sensors using SlingBAG takes less than 4 hours, while the memory overflows for k-Wave at this scale. The significant improvement in both reconstruction range and speed is largely attributable to the adaptive point cloud representation, which inherently aligns better with the sparsity characteristics typically found in real PA sources. Considering both physical model accuracy and computational cost, the point cloud representation provides a more efficient description of photoacoustic signal sources than voxel representation. Additionally, our differentiable rapid radiator ensures that both the forward simulation and the backward gradient propagation are fully differentiable, enabling rapid parameter updates and convergence.

SlingBAG demonstrates high precision. Comparing the reconstruction results to simulated acoustic sources reveals excellent localization and numerical accuracy in reconstructing photoacoustic sources. The 3D PAI results from SlingBAG can also be used to generate temporal signals for sensors at new positions (Supplementary Fig. 2), indicating great potential for fast sensor interpolation research for PAI. We introduce an indirect method for converting point cloud results to voxel grids in the supplementary material. The high reconstruction accuracy is attributable to two factors: (1) point cloud models allow the source to converge to finer spatial locations, and (2) the high accuracy of the forward simulation used in the differentiable rapid radiator of the SlingBAG algorithm, which accurately describes the PA wave propagation, as validated by comparisons with k-Wave simulation results (Supplementary Fig. 1). Furthermore, the computational steps are completely differentiable, facilitating easy gradient propagation and parameter updates.

It is worth noting that the multi-order spherical discretization strategy utilized in our differentiable rapid radiator is general, where specific discretization approaches are not unique. The coefficients for the 10th-order spherical discretization provided in

this work are based on the three-sigma rule from Gaussian distribution in statistics, which could be extended to higher orders to enhance model accuracy, albeit at the cost of increased computational demand. Since comparisons with k-Wave have shown that the precision of 10th-order is sufficient, all studies in this work were conducted under the condition of 10th-order discretization.

In addition to investigating sparse detector configurations, we also explored the 3D reconstruction performance of the SlingBAG algorithm under severe limited view conditions, using both simulated hand signals (Supplementary Fig. 4) and real mouse brain signals (Supplementary Fig. 5-7). The results indicate that, under severe loss of PA signals in vast acquisition angle, the continuity of the SlingBAG reconstruction significantly deteriorates — even denser sensor arrangements cannot compensate for the loss of angular information. Interestingly, when using the indirect method to convert point cloud results into voxel grids — specifically, by simulating point cloud results using our forward model to interpolate dense sensor signals under limited angles and then performing UBP reconstruction — we observe a visual mitigation of the continuity degradation caused by missing angles. However, when performing full-angle interpolation for this indirect method, the reconstruction results approach those obtained from directly converting point clouds into voxel grids. This suggests that indirect methods can provide a practical means of reducing the visual impact of angle loss, yet ultimately, full-angular information remains essential for maintaining the highest possible reconstruction quality.

It is important to point out that the learning rate during the iterative process has a significant impact on the model’s convergence speed and reconstruction quality. We recommend setting the learning rate for peak initial pressure and standard deviation to 0.05 and 0.00004, respectively, during the coarse reconstruction phase. For the fine reconstruction phase, the learning rates for the 3D coordinates, peak initial pressure, and standard deviation should be set to 0.000004, 0.004, and 0.000004, respectively. Interestingly, during the real mouse brain reconstruction process, we observed that further reducing the learning rate could decrease the loss, but the overall image quality deteriorated instead, with more noise introduced. This phenomenon occurs because, under excessively small learning rates, the model tends to reconstruct the noise present in the original signal, resulting in noisier reconstructions.

Despite SlingBAG’s advantages, it currently assumes a homogeneous, non-viscous medium. In vivo studies, however, often involve non-negligible heterogeneities in sound velocity. Future work will address this by either (1) partitioning the reconstruction space based on prior knowledge of sound speed distribution, applying different speeds to sources in different regions, or (2) introducing a learnable sound speed parameter for each point in the point cloud, where each point forms a sphere with uniform sound speed within it. This would incorporate sound speed as an additional optimization parameter.

Since the differentiable radiator in the SlingBAG algorithm is based on a multi-order spherical discretization strategy in 3D space, it is currently not suited for 2D PACT. However, extending the SlingBAG algorithm to linear US array configurations is feasible. This would involve using multiple concentric cylinder analytical solutions to discretize the forward propagation results of Gaussian-distributed circular acoustic

sources, similar to the 3D strategy, resulting in 2D planes of point clouds rather than 3D spaces. Given that sensor sparsity issues primarily arise in 3D array configurations for 3D photoacoustic imaging, we have not focused extensively on PAT in this paper, but we will explore this further in future work.

Inherited from unique IR superior characteristics, the SlingBAG algorithm is highly versatile to be easily applied to a variety of array shapes such as planar arrays, spherical arrays, as well as a vast customized geometric configuration, making it a powerful 3D PAI reconstruction algorithm. Furthermore, the exceptional imaging quality of the SlingBAG algorithm and much fewer demands in computing resources will foster large-scale 3D PA imaging implementations, such as whole-body small animal imaging, fast clinical entire foot peripheral vascular imaging, and 3D PA breast or thyroid tumor imaging. Besides, as the superior performance of the SlingBAG algorithm for extreme sparse US sensors, this approach can also substantially reduce PAI system costs, fostering its wide implementations.

4 Methods

4.1 Differentiable Rapid Radiator Based on Multi-Order Spherical Discretization of Gaussian-distributed Spherical Photoacoustic Source

In the field of computer graphics, rendering describes the forward process of converting the shape, color, and material of a 3D scene into a 2D image. Conversely, reconstruction is the inverse process that restores 3D scene shape, color, and material from 2D images. Differentiable rendering, characterized by its differentiable rendering process, enables the computation of image gradients and the optimization of 3D scene parameters through methods like gradient descent, further facilitating the restoration of 3D scenes. Differentiable rendering is foundational for high-quality 3D scene rapid reconstruction technologies such as NeRF and 3D Gaussian splatting. The rendering equation used in light rendering simulates the propagation of light within a scene based on edge sampling Monte Carlo path-tracing methods. However, the acoustic radiation process in photoacoustic imaging differs significantly.

Corresponding to 3D vision, the forward process in PA imaging describes the propagation of ultrasound waves from PA signal sources with initial PA pressure to the transducer’s reception, resulting in temporal acoustic signals. The inverse process reconstructs the initial PA pressure at the acoustic source from these received temporal signals. Since the initial PA pressure is proportionate to the light absorption coefficient of the source, the distribution of the initial PA pressure can be considered a morphological feature of the light-absorbing tissue.

K-Wave [39] is a widely used simulation toolkit in the PA imaging field. It numerically solves the wave equation using the pseudo-spectral method to obtain temporal pressure signals at all grid spatial positions from the initial PA sources. This method provides high simulation accuracy and supports extensive application scenarios by allowing settings for various medium acoustic properties, including heterogeneous sound velocity distributions. However, this method requires substantial storage space

when a large-scale grid is needed to cover from the source to the remote sensor array. Although it works well for 2D PAI, it faces severe challenges for researchers to apply this simulation toolkit in 3D reconstruction methods. Additionally, the forward propagation process using the pseudo-spectral method does not support direct gradient back-propagation, limiting its performance in iterative reconstruction methods.

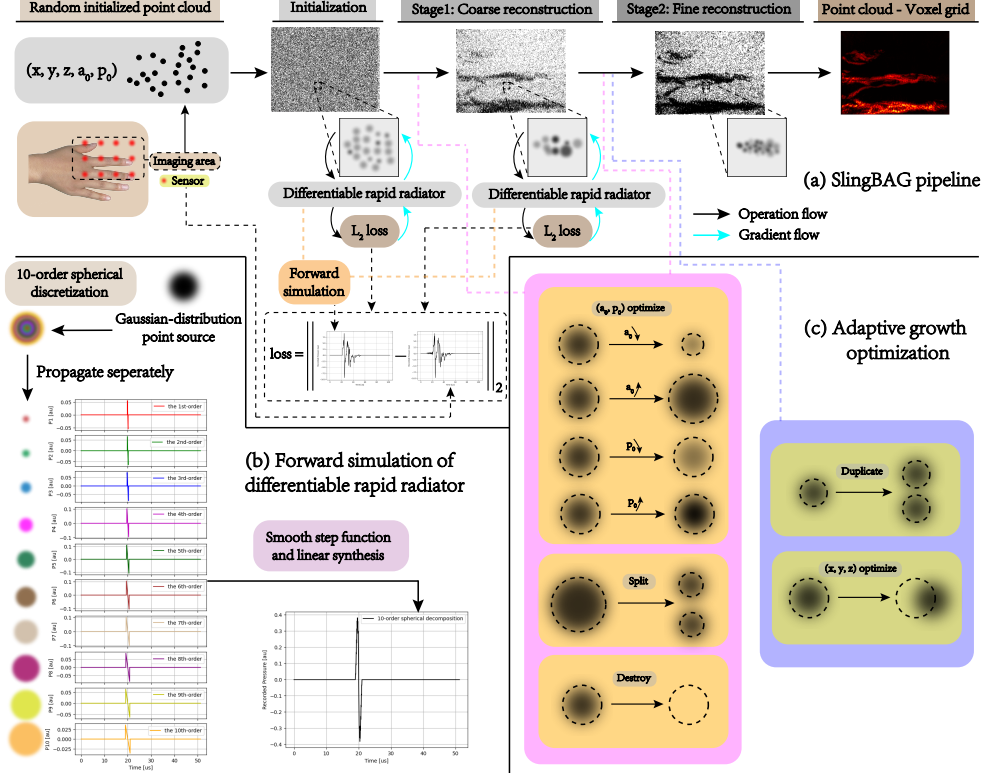


Fig. 7 The overview framework of Sliding Gaussian Ball Adaptive Growth algorithm. (a) The SlingBAG pipeline. (b) The forward simulation of differentiable rapid radiator. (c) Adaptive growth optimization based on iterative point cloud.

Inspired by differentiable rendering techniques from computer graphics, and based on the fundamental principles of PA imaging, we propose the concept of “differentiable acoustic radiation” and introduce a unique differentiable rapid radiator for PA imaging. The entire process is fully differentiable and friendly to parallel computing. As compared with k-wave in supplementary, it achieves a similarity of over 99.5% , while three orders of magnitude faster in simulation speed.

This model uses a series of isotropic Gaussian-distributed PA sources to explicitly represent 3D PA scenes, with each Gaussian PA source characterized by three attributes: its peak initial pressure p_0 , standard deviation a_0 , and 3D coordinates

(x_s, y_s, z_s) (i.e., the mean of the spherical Gaussian distribution). These attributes are stored in the form of point cloud and iteratively updated during the reconstruction process. The entire PA propagation is viewed as a linear superposition of the independent PA wave propagation of all Gaussian PA sources within the scene. Each Gaussian PA source is a linear combination of multi-order concentric homogeneous spheres, which follows the three-sigma rule of Gaussian distribution. For each sphere, its initial pressure and radius are computed based on the peak initial pressure p_0 , standard deviation a_0 , combined with fixed weights—a process referred to as multi-order spherical discretization. The reason to choose spherical shape is that the propagation equation of a homogeneous spherical PA source has an analytical solution, which helps to build a rapid differentiation radiator. We demonstrate the forward simulation of our differentiable rapid radiator in Fig. 7(b).

(i) Forward Simulation. For a Gaussian PA source with peak initial pressure p_0 , standard deviation a_0 , and 3D coordinates (x_s, y_s, z_s) , we detail the parameters of its 10th-order concentric spherical discretization: The centers of all 10 spheres are located at (x_s, y_s, z_s) , and their radii and initial sound pressures distributed on each sphere are as follows in Tab. 1:

Table 1 Radii and pressures of 10 spheres

Radius	$0.5a_0$	$0.6a_0$	$0.9a_0$	$1.2a_0$	$1.5a_0$	$1.8a_0$	$2.1a_0$	$2.4a_0$	$2.7a_0$	$3.0a_0$
Pressure	$\frac{10}{55}p_0$	$\frac{9}{55}p_0$	$\frac{8}{55}p_0$	$\frac{7}{55}p_0$	$\frac{6}{55}p_0$	$\frac{5}{55}p_0$	$\frac{4}{55}p_0$	$\frac{3}{55}p_0$	$\frac{2}{55}p_0$	$\frac{1}{55}p_0$

It is worth noting that this discretization method is not unique. The choice of the 10th-order balances model accuracy and computational complexity. Using higher-order spherical discretization can further improve computational accuracy, but the computational load will increase linearly with the order.

The analytical solution for the PA wave propagation of a uniform sphere PA source excited by a Dirac laser pulse [40] is:

$$p(R, t) = p_0 \frac{R - v_s t}{2R} (u(R - v_s t + a_0) - u(R - v_s t - a_0)),$$

$$\text{where } R = \sqrt{(x_r - x_s)^2 + (y_r - y_s)^2 + (z_r - z_s)^2}, \quad (1)$$

$$u(x) = \begin{cases} 0, & x < 0 \\ 1, & x \geq 0 \end{cases}, \quad \delta(x) = \frac{d}{dx}u(x),$$

where (x_s, y_s, z_s) is the position of the sphere's center, v_s is the speed of sound, t is the propagation time, p_0 is the initial acoustic pressure of the sphere, a_0 is the radius of the sphere, (x_r, y_r, z_r) is the sensor coordinate, R is the Euclidean distance between the sensor to the center of the sphere (thus $R > a_0$), and $u(x)$ is the unit step function.

Based on the analytical solution and superposition of waves from all concentric spheres, we can derive the 10th-order spherical acoustic pressure propagation expression $P_{10\text{ball}}$. The received acoustic pressure signal at any spatial location is obtained by the linear superposition of the acoustic pressure propagation expressions from all Gaussian spherical sources.

Due to the presence of the unit step function $u(x)$, the 10th-order spherical discretization is not differentiable yet. To address this, we use the following differentiable formula to approximate the unit step function $u(x)$ with high precision:

$$u_\epsilon(x) = \frac{1}{2}(1 + \text{erf}(\epsilon x)), \quad (2)$$

$$\text{where } \text{erf}(x) = \frac{2}{\sqrt{\pi}} \int_0^x e^{-t^2} dt.$$

Considering the typical resolution of PA imaging, which ranges from 100 μm to 1 mm, we set the smoothness factor ϵ to 10^6 to ensure convergence to the unit step function.

Thus, we obtain the acoustic pressure propagation expression for a Gaussian spherical source with peak initial pressure p_0 , standard deviation a_0 and spatial coordinates (x_s, y_s, z_s) based on the 10th-order spherical discretization:

$$p(R, t) = \sum_{i=1}^{10} p_0^i \frac{D}{2R} (u_\epsilon(D + a_0^i) - u_\epsilon(D - a_0^i)), \quad (3)$$

$$\text{where } D = R - v_s t,$$

where a_0^i and p_0^i are the radius and initial pressure of the i th-order sphere in Tab. 1. In each step of the calculation, it is fully differentiable.

(ii) Backward Propagation. After representing our forward prediction using a smooth step function, our forward prediction function $p(R, t)$ becomes fully differentiable, and the derivative of our smooth step function is:

$$\delta_\epsilon(x) = \frac{d}{dx} u_\epsilon(x) = \frac{\epsilon}{\sqrt{\pi}} \exp(-\epsilon^2 x^2), \quad (4)$$

which is also a good approximation of the Dirac delta function $\delta(x)$.

Thus, in the end-to-end training process, we need to compute the derivatives of $p(R, t)$ with respect to the peak initial pressure p_0 , standard deviation a_0 , and the spatial center coordinates (x_s, y_s, z_s) to propagate the gradient backward. Taking the partial derivative of Eq.(3), we can get:

$$\begin{aligned}
\frac{\partial p}{\partial p_0} &= \sum_{i=1}^{10} \frac{p_0^i}{p_0} \frac{D}{2R} (u_\epsilon(D + a_0^i) - u_\epsilon(D - a_0^i)), \\
\frac{\partial p}{\partial a_0} &= \sum_{i=1}^{10} \frac{a_0^i}{a_0} p_0^i \frac{D}{2R} (\delta_\epsilon(D + a_0^i) + \delta_\epsilon(D - a_0^i)), \\
\frac{\partial p}{\partial x_s} &= \left(\frac{\partial p}{\partial R} + \frac{\partial p}{\partial D} \frac{\partial D}{\partial R} \right) \frac{\partial R}{\partial x_s} \\
&= -\frac{x_r - x_s}{R} \sum_{i=1}^{10} p_0^i \left(\frac{v_s t}{2R^2} (u_\epsilon(D + a_0^i) - u_\epsilon(D - a_0^i)) \right. \\
&\quad \left. + \frac{D}{2R} (\delta_\epsilon(D + a_0^i) - \delta_\epsilon(D - a_0^i)) \right).
\end{aligned} \tag{5}$$

The derivatives with respect to y_s and z_s are similar to the derivative with respect to x_s shown above. The above expression demonstrates the back-propagation computation of our differentiable rapid radiator. Both forward and backward models are implemented with GPU-accelerated code based on Taichi [41] and pure CUDA syntax.

4.2 Sliding Gaussian Ball Adaptive Growth Point Cloud Model

The overview framework of Sliding Gaussian Ball Adaptive Growth algorithm is given in Fig. 7(a). We start by randomly initializing the point cloud within the field of view. All attributes of each point are randomly sampled from a uniform distribution within a certain range. This randomly initialized point cloud serves as the initial PA source. Using our differentiable rapid radiator, the acoustic signals received at the sensor locations can be simulated. By calculating the loss between these simulated signals and the actual sensor data and performing gradient back-propagation, the model then updates all attributes of the points in the point cloud. All the optimization methods of each point in the point cloud are demonstrated in Fig. 7(c).

It is important to emphasize that the IR reconstruction contains two successive reconstruction stages: coarse reconstruction stage and fine reconstruction stage. In the first stage, only the standard deviation and peak initial acoustic pressures are updated, while the spatial coordinates of the points remain unchanged, and the model's duplication feature is not activated. This stage helps to achieve rapid convergence while maintaining computational efficiency.

Then, after a certain number of iterations, the model undergoes adaptive density optimization of the point cloud to ensure computational efficiency and prevent convergence to sub-optimal solutions that violate physical principles. Points with excessively low peak initial acoustic pressure or standard deviation values are discarded to maximize resource savings and expedite iteration speed. For points with excessively large standard deviation values, the model performs a splitting operation. This involves

Algorithm 1 SlingBAG

Input: Z_0 : Randomly initialized point cloud

S_0 : Real signal

(x, y, z, a_0, p_0) : Attributes of each point

Output: 3D reconstruction result in form of voxel grid

```
1:  $Z_1 = Z_0$ 
2: while not converged do ▷ Coarse reconstruction stage
3:   Generate signal  $S_1$  by forward simulation with differentiable rapid radiator
4:   Calculate loss:  $L = \|S_1 - S_0\|_2$ 
5:   Gradient back-propagate by differentiable rapid radiator:  $\frac{\partial L}{\partial a_0}, \frac{\partial L}{\partial p_0}$ 
6:   Update on  $(a_0, p_0)$ 
7:   Perform splitting and destroying of points in  $Z_1$ 
8: end while
9:  $Z_2 = Z_1$ 
10: while not converged do ▷ Fine reconstruction stage
11:   Generate signal  $S_2$  by forward simulation with differentiable rapid radiator
12:   Calculate loss:  $L = \|S_2 - S_0\|_2$ 
13:   Gradient back-propagate by differentiable rapid radiator:  $\frac{\partial L}{\partial x}, \frac{\partial L}{\partial y}, \frac{\partial L}{\partial z}, \frac{\partial L}{\partial a_0}, \frac{\partial L}{\partial p_0}$ 
14:   Update on  $(x, y, z, a_0, p_0)$ 
15:   Perform duplicating, splitting and destroying of points in  $Z_2$ 
16: end while
17: for each point in  $Z_2$  do ▷ Point cloud to voxel grid
18:   Convert into voxel grid through point cloud-voxel grid shader
19: end for
```

splitting an initially large sphere into two smaller spheres, each with half the original radius, while maintaining the same peak initial acoustic pressure. The spatially splitting direction is aligned with the gradient direction of the point position.

As the loss begins to converge, the model further enhances its capabilities by incorporating position coordinate updates into the optimizer alongside updates for peak initial acoustic pressure and standard deviations, and the point cloud enters into the fine reconstruction stage. The model then activates its duplication feature at specific iteration counts, enabling all points in the current point cloud to be duplicated along their respective position gradients. This approach increases the point cloud’s density and allows for more precise control and fine-tuning of each point, leading to more detailed and accurate 3D reconstructions.

Through these processes, the model can further refine the point cloud, improving the resolution and detail of the 3D reconstruction. This adaptive and iterative approach facilitates high-quality 3D PA imaging reconstructions even under conditions of extremely sparse sensor distributions.

4.3 Physically-Based Point Cloud to Voxel Grid Shader

While the 3D point cloud resulting from iterative processing encapsulates all the information about the reconstructed PA sources, directly visualizing it does not effectively

convey each point’s standard deviation and peak initial acoustic pressure. Since voxel grids are widely used for 3D visualization of PA imaging results, we then continue to develop a converter, termed the “Point Cloud to Voxel Grid Shader”, which transforms point cloud data into voxel grid information.

Due to the density of the point cloud, its coordinates may not be perfectly aligned with the voxel grid nodes. The shader first aligns the voxel grid coordinate space with the point cloud coordinate space in three dimensions. Next, it iterates over all the points in the point cloud, reading each point’s peak initial acoustic pressure and standard deviation, which correspond to the gray-scale intensity and brush size, respectively. These attributes are refined using the discretization coefficients from the 10th-order spherical discretization used in the differentiable rapid radiator.

Here’s a detailed breakdown of the conversion process:

1. Alignment of Coordinate Spaces: The voxel grid coordinate space and the point cloud coordinate space are aligned in 3D space to ensure accurate correspondence.
2. Reading Point Attributes: For each point in the point cloud, the shader reads the peak initial acoustic pressure and standard deviation information. These attributes, representing gray-scale intensity and brush size, are adjusted based on the coefficients from the 10th-order spherical discretization.
3. Voxel Grid Coloring: The shader “paints” each point into the 3D space using the adjusted gray-scale intensity and brush size. The markings interact with the voxel grid, mapping the gray-scale intensity onto the grid nodes. Intensity values at the voxel grid nodes are accumulated when multiple brushstrokes overlap, ensuring a complete rendering of the voxel grid from the point cloud data.

By converting point cloud data into a voxel grid using this physically-based point cloud to voxel grid shader, we achieve comprehensive and detailed 3D visualization that accurately reflects the initial acoustic pressures and resolutions from the original point cloud data. This method leverages the strengths of both point cloud and voxel grid representations, enhancing visualization for analysis and interpretation in the field of PA imaging.

Acknowledgements

This research was supported by the following grants: the National Key R&D Program of China (No. 2023YFC2411700, No. 2017YFE0104200); the Beijing Natural Science Foundation (No. 7232177); the Basic Science Research Program through the National Research Foundation of Korea (NRF) funded by the Ministry of Education (2020R1A6A1A03047902).

We would like to express our gratitude to Professor Chao Tian and Mr. Zhijian Tan from the University of Science and Technology of China for their selfless support.

Declarations

Funding

The National Key R&D Program of China (No. 2023YFC2411700, No. 2017YFE0104200); the Beijing Natural Science Foundation (No. 7232177); the Basic Science Research Program through the National Research Foundation of Korea (NRF) funded by the Ministry of Education (2020R1A6A1A03047902).

Competing interests

All authors declare no competing interests.

References

- [1] Park, J., Choi, S., Knieling, F., Clingman, B., Bohndiek, S., Wang, L.V., Kim, C.: Clinical translation of photoacoustic imaging. *Nature Reviews Bioengineering*, 1–20 (2024)
- [2] Matsumoto, Y., Asao, Y., Yoshikawa, A., Sekiguchi, H., Takada, M., Furu, M., Saito, S., Kataoka, M., Abe, H., Yagi, T., *et al.*: Label-free photoacoustic imaging of human palmar vessels: a structural morphological analysis. *Scientific reports* **8**(1), 786 (2018)
- [3] Matsumoto, Y., Asao, Y., Sekiguchi, H., Yoshikawa, A., Ishii, T., Nagae, K.-i., Kobayashi, S., Tsuge, I., Saito, S., Takada, M., *et al.*: Visualising peripheral arterioles and venules through high-resolution and large-area photoacoustic imaging. *Scientific reports* **8**(1), 14930 (2018)
- [4] Ivankovic, I., Merčep, E., Schmedt, C.-G., Deán-Ben, X.L., Razansky, D.: Real-time volumetric assessment of the human carotid artery: handheld multispectral optoacoustic tomography. *Radiology* **291**(1), 45–50 (2019)
- [5] Deán-Ben, X.L., Razansky, D.: Portable spherical array probe for volumetric real-time optoacoustic imaging at centimeter-scale depths. *Optics express* **21**(23), 28062–28071 (2013)
- [6] Nagae, K., Asao, Y., Sudo, Y., Murayama, N., Tanaka, Y., Ohira, K., Ishida, Y., Otsuka, A., Matsumoto, Y., Saito, S., *et al.*: Real-time 3d photoacoustic visualization system with a wide field of view for imaging human limbs. *F1000Research* **7** (2018)
- [7] Kim, W., Choi, W., Ahn, J., Lee, C., Kim, C.: Wide-field three-dimensional photoacoustic/ultrasound scanner using a two-dimensional matrix transducer array. *Optics Letters* **48**(2), 343–346 (2023)
- [8] Piras, D., Xia, W., Steenbergen, W., Van Leeuwen, T.G., Manohar, S.: Photoacoustic imaging of the breast using the twente photoacoustic mammoscope:

- present status and future perspectives. *IEEE Journal of Selected Topics in Quantum Electronics* **16**(4), 730–739 (2009)
- [9] Heijblom, M., Piras, D., Xia, W., Van Hespén, J., Klaase, J., Engh, F., Van Leeuwen, T., Steenbergen, W., Manohar, S.: Visualizing breast cancer using the twente photoacoustic mammoscope: what do we learn from twelve new patient measurements? *Optics express* **20**(11), 11582–11597 (2012)
- [10] Li, S., Zhang, G., Wang, Y., Li, W., Sun, Y., Li, C.: Photoacoustic imaging of peripheral vessels in extremities by large-scale synthetic matrix array. *Journal of Biomedical Optics* **29**(S1), 11519–11519 (2024)
- [11] Wang, Y., Li, C.: Comprehensive framework of gpu-accelerated image reconstruction for photoacoustic computed tomography. *Journal of Biomedical Optics* **29**(6), 066006–066006 (2024)
- [12] Paltauf, G., Viator, J., Prah, S., Jacques, S.: Iterative reconstruction algorithm for optoacoustic imaging. *The Journal of the Acoustical Society of America* **112**(4), 1536–1544 (2002)
- [13] Wang, K., Su, R., Oraevsky, A.A., Anastasio, M.A.: Investigation of iterative image reconstruction in three-dimensional optoacoustic tomography. *Physics in Medicine & Biology* **57**(17), 5399 (2012)
- [14] Huang, C., Wang, K., Nie, L., Wang, L.V., Anastasio, M.A.: Full-wave iterative image reconstruction in photoacoustic tomography with acoustically inhomogeneous media. *IEEE transactions on medical imaging* **32**(6), 1097–1110 (2013)
- [15] Shang, R., Archibald, R., Gelb, A., Luke, G.P.: Sparsity-based photoacoustic image reconstruction with a linear array transducer and direct measurement of the forward model. *Journal of biomedical optics* **24**(3), 031015–031015 (2019)
- [16] Zhu, J., Huynh, N., Ogunlade, O., Ansari, R., Lucka, F., Cox, B., Beard, P.: Mitigating the limited view problem in photoacoustic tomography for a planar detection geometry by regularized iterative reconstruction. *IEEE Transactions on Medical Imaging* **42**(9), 2603–2615 (2023)
- [17] Arridge, S.R., Betcke, M.M., Cox, B.T., Lucka, F., Treeby, B.E.: On the adjoint operator in photoacoustic tomography. *Inverse Problems* **32**(11), 115012 (2016)
- [18] Hauptmann, A., Lucka, F., Betcke, M., Huynh, N., Adler, J., Cox, B., Beard, P., Ourselin, S., Arridge, S.: Model-based learning for accelerated, limited-view 3-d photoacoustic tomography. *IEEE transactions on medical imaging* **37**(6), 1382–1393 (2018)
- [19] Huynh, N., Zhang, E., Francies, O., Kuklis, F., Allen, T., Zhu, J., Abeyakoon, O., Lucka, F., Betcke, M., Jaros, J., et al.: A fast all-optical 3d photoacoustic scanner

for clinical vascular imaging. *Nature Biomedical Engineering*, 1–18 (2024)

- [20] Hauptmann, A., Cox, B.: Deep learning in photoacoustic tomography: current approaches and future directions. *Journal of Biomedical Optics* **25**(11), 112903–112903 (2020)
- [21] Zheng, W., Zhang, H., Huang, C., Shijo, V., Xu, C., Xu, W., Xia, J.: Deep learning enhanced volumetric photoacoustic imaging of vasculature in human. *Advanced Science* **10**(29), 2301277 (2023)
- [22] Mildenhall, B., Srinivasan, P.P., Tancik, M., Barron, J.T., Ramamoorthi, R., Ng, R.: Nerf: Representing scenes as neural radiance fields for view synthesis. *Communications of the ACM* **65**(1), 99–106 (2021)
- [23] Kerbl, B., Kopanas, G., Leimkühler, T., Drettakis, G.: 3d gaussian splatting for real-time radiance field rendering. *ACM Transactions on Graphics* **42**(4) (2023)
- [24] Weiss, S., Westermann, R.: Differentiable direct volume rendering. *IEEE Transactions on Visualization and Computer Graphics* **28**(1), 562–572 (2021)
- [25] Yariv, L., Gu, J., Kasten, Y., Lipman, Y.: Volume rendering of neural implicit surfaces. *Advances in Neural Information Processing Systems* **34**, 4805–4815 (2021)
- [26] Barron, J.T., Mildenhall, B., Tancik, M., Hedman, P., Martin-Brualla, R., Srinivasan, P.P.: Mip-nerf: A multiscale representation for anti-aliasing neural radiance fields. In: *Proceedings of the IEEE/CVF International Conference on Computer Vision*, pp. 5855–5864 (2021)
- [27] Chen, A., Xu, Z., Geiger, A., Yu, J., Su, H.: Tensorf: Tensorial radiance fields. In: *European Conference on Computer Vision*, pp. 333–350 (2022). Springer Nature Switzerland Cham
- [28] Yao, Y., Zhang, J., Liu, J., Qu, Y., Fang, T., McKinnon, D., Tsin, Y., Quan, L.: Neilf: Neural incident light field for physically-based material estimation. In: *European Conference on Computer Vision*, pp. 700–716 (2022). Springer
- [29] Müller, T., Evans, A., Schied, C., Keller, A.: Instant neural graphics primitives with a multiresolution hash encoding. *ACM transactions on graphics (TOG)* **41**(4), 1–15 (2022)
- [30] Yao, B., Zeng, Y., Dai, H., Wu, Q., Xiao, Y., Gao, F., Zhang, Y., Yu, J., Cai, X.: Sparse-view signal-domain photoacoustic tomography reconstruction method based on neural representation. *arXiv preprint arXiv:2406.17578* (2024)
- [31] Kerbl, B., Kopanas, G., Leimkühler, T., Drettakis, G.: 3d gaussian splatting for real-time radiance field rendering. *ACM Trans. Graph.* **42**(4), 139–1 (2023)

- [32] Zwicker, M., Pfister, H., Van Baar, J., Gross, M.: Ewa splatting. *IEEE Transactions on Visualization and Computer Graphics* **8**(3), 223–238 (2002)
- [33] Choi, S., Yang, J., Lee, S.Y., Kim, J., Lee, J., Kim, W.J., Lee, S., Kim, C.: Deep learning enhances multiparametric dynamic volumetric photoacoustic computed tomography in vivo (dl-pact). *Advanced Science* **10**(1), 2202089 (2023)
- [34] Choi, W., Park, B., Choi, S., Oh, D., Kim, J., Kim, C.: Recent advances in contrast-enhanced photoacoustic imaging: overcoming the physical and practical challenges. *Chemical Reviews* **123**(11), 7379–7419 (2023)
- [35] Kim, J., Lee, J., Choi, S., Lee, H., Yang, J., Jeon, H., Sung, M., Kim, W.J., Kim, C.: 3d multiparametric photoacoustic computed tomography of primary and metastatic tumors in living mice. *ACS nano* (2024)
- [36] Kim, J., Kim, G., Li, L., Zhang, P., Kim, J.Y., Kim, Y., Kim, H.H., Wang, L.V., Lee, S., Kim, C.: Deep learning acceleration of multiscale superresolution localization photoacoustic imaging. *Light: science & applications* **11**(1), 131 (2022)
- [37] Park, J., Choi, S., Knieling, F., Clingman, B., Bohndiek, S., Wang, L.V., Kim, C.: Clinical translation of photoacoustic imaging. *Nature Reviews Bioengineering* (in press)
- [38] Beck, A., Teboulle, M.: Fast gradient-based algorithms for constrained total variation image denoising and deblurring problems. *IEEE transactions on image processing* **18**(11), 2419–2434 (2009)
- [39] Treeby, B.E., Cox, B.T.: k-wave: Matlab toolbox for the simulation and reconstruction of photoacoustic wave fields. *Journal of biomedical optics* **15**(2), 021314–021314 (2010)
- [40] Xu, M., Wang, L.V.: Universal back-projection algorithm for photoacoustic computed tomography. *Physical Review E—Statistical, Nonlinear, and Soft Matter Physics* **71**(1), 016706 (2005)
- [41] Hu, Y., Li, T.-M., Anderson, L., Ragan-Kelley, J., Durand, F.: Taichi: a language for high-performance computation on spatially sparse data structures. *ACM Transactions on Graphics (TOG)* **38**(6), 201 (2019)